Automated data-based damage localization under ambient vibration using local modal filters and dynamic strain measurements: Experimental applications

Gilles Tondreau *, Arnaud Deraemaeker

ULB, Building Architecture and Town Planning, 50 av. Franklin Roosevelt, CP 194/02, B-1050 Brussels, Belgium

A R T I C L E   I N F O

A B S T R A C T

This paper deals with the experimental application of modal filters for automated damage localization using dynamic strain measurements. Previously developed for damage detection, the extension of modal filtering to damage localization consists in splitting a very large network of dynamic strain sensors into several independent local sensor networks. An efficient signal processing coupled to control charts allows a fully automated data-based damage localization once the modal filters are initialized. The method is tested experimentally on a small clamped-free steel plate and a 3.78 m long steel I-beam, both instrumented with a network of cheap piezoelectric patches to measure the dynamic strains. A removable damage is introduced at different positions by means of a small removable damage device. For both applications, the method can successfully detect and locate all damage cases considered, showing the potentiality of the method for field applications.

© 2014 Elsevier Ltd. All rights reserved.

1. Introduction

Bridges tend to be exposed to higher loads due to heavier traffic, are aging which possibly leads to loss of concrete or fatigue cracks [1], and can be subjected to casual events such as earthquakes or collisions. All those phenomena can be at the origin of damage, which explains the real interest in developing methods for assessing continuously the integrity of structures in (near) real time. An optimal maintenance of civil engineering structures requires to identify damage at an early stage, since small and frequent repairs are much less costly than major repairs or total rebuilding after collapse. Current practice for the monitoring of structures consists in scheduled maintenance based on local methods such as eddy current, visual inspections or ultrasounds [2]. All these methods suffer from the same drawbacks: they require that the vicinity of the damage is known and accessible, they are time consuming and expensive. Moreover, these techniques are not automated and subjective. Indeed, a report of the U.S. Department of Transportation [3] points out that many factors can affect visual inspection, leading to condition ratings varying strongly from one technician to another. Pines and Aktan discuss in [4] the main difficulties related to scheduled maintenance of long-span bridges, but the major problem is the non-continuous monitoring provided by this approach. An undetected critical damage appearing between two inspections can lead to a catastrophic structural failure, as in the case of the I-35W Mississippi River Bridge which collapsed despite annual inspection [5].

* Corresponding author.
  E-mail addresses: gilles.tondreau@ulb.ac.be (G. Tondreau), aderaema@ulb.ac.be (A. Deraemaeker).

For aesthetics reasons as well as a more rational use of building materials, the bridges are becoming lighter and more slender, increasing the levels of vibrations under ambient excitation despite the fact that passive, active and hybrid damping solutions are proposed [6,7]. While these levels of vibrations can be detrimental to the lifetime of the structures due to fatigue, they can also be used for continuous monitoring. The basic idea is that damage affects the stiffness which in turn affects the vibration characteristics. Based on this concept, vibration-based structural health monitoring (SHM) has gained an increasing attention in the last few decades, using mainly eigenfrequencies, damping ratios and modes shapes for damage assessment [8]. The reason of this popularity is the ease of measuring modal parameters or frequency responses on real structures thanks to recent advances in sensing systems (increase of cost-effective computing memory and speed [9–11]), and in operational modal analysis (OMA, [12,13]).

Rytter [14] has proposed a hierarchical decomposition of the SHM process in four levels, which has been widely accepted in the SHM literature: detection (level 1), location (level 2) and quantification (level 3) of the damage, as well as prediction of the remaining service life of the damaged structure (level 4). As the level increases, the knowledge about the damage increases and, usually, the complexity of the method increases as well. A distinction can be made between the data-based and the model-based method. The data-based methods present the important advantage of avoiding the need to construct a detailed physical numerical model of the structure. Supervised methods are data-based methods which require measurements in the damaged state, and can possibly quantify the damage, while unsupervised methods can at best locate the damage by comparing the current measurements with undamaged measurements. Model-based methods use physical numerical models which are updated based on the measured signals. Such techniques can possibly reach up to level 4 of SHM, but are much more computationally expensive than data-based methods [15–17]. For civil engineering structures, physical numerical models with a sufficient accuracy can be very difficult to achieve, and measurements in a damaged state are usually not available, so that unsupervised data-based methods are better suited for this type of application.

Despite the very large scientific literature on the subject [18,8], SHM technologies have not yet been applied successfully to real industrial applications in civil engineering structures due to major difficulties. The first one is that the damage is typically a local phenomenon, which means that only important damage levels will be detected if one looks at global dynamic properties such as the eigenfrequencies [19]. The second one is that the structures are subjected to ambient excitation such as traffic or wind. The vibration levels are rather low and instrumentation has to be very sensitive in order to measure them with a good accuracy. The third one is the problem of automation and robustness of the SHM system against sensor failure and variability (temperature effects, boundary condition effects, humidity, etc.) [20,21]. In addition, non-technical issues such as economic benefits that can be expected from SHM systems have to be further investigated in order to convince structure owners of the interest of such approaches.

In order to avoid the high computational costs associated to model-based methods and to take into account the usual lack of training data from damaged civil engineering structures, a new fully automated data-based unsupervised technique for damage localization was developed in [22]. The method is based on an automated feature extraction process using the so-called modal filters [23] which is computationally very cheap. Initially developed in the context of damage detection in [24,25] with accelerometers, this technique exploits only sensor responses, and it has been shown to be relatively robust to environmental changes [26] which can cause significant changes in modal properties [27]. The experimental damage detection on a small aircraft wing using modal filters with accelerometers has been illustrated in [28]. On the contrary to the work of Mendrok and Uhl [29], the extension of modal filters to damage localization proposed in [22] consists in using in service dynamic strain measurements to locate small damage instead of accelerations. This choice of sensing technology is justified by the fact that strains have been demonstrated to be locally sensitive to damage, as discussed both numerically and experimentally in [30–32]. Control charts [33,34] are used to detect automatically a change from the normal healthy condition, based on the extracted damage sensitive features. The automation of the process is a key point for a successful implementation of continuous monitoring systems. The method has been applied successfully to automatically locate very small damage (only 2 percent of stiffness reduction over 1/100th of the length of the structure) on a simply supported beam as well as on a complex 3D model inspired from a real bridge. The present paper investigates the experimental validation of this new technique on two laboratory experiments.

This paper is organized as follows: Section 2 shortly describes the method based on modal filters for automated damage localization using output-only measurements. A new damage sensitive feature is proposed and the novelty detection using univariate and multivariate control charts is also detailed. Section 3 presents two experimental applications of the method: the first example is a small clamped-free steel plate instrumented with 8 cheap piezoelectric patches and excited with a piezoceramic patch, while the second application deals with a 3.78 m long steel I-beam on which 20 cheap piezoelectric patches are installed and it is excited with an electro-dynamic shaker. In both examples, a removable damage is simulated by fixing a small removable damage device at different positions. The experimental results confirm the numerical predictions and show the very good potential performances of the proposed method for application on real cases.

2. Damage localization using modal filters

Initially developed for damage detection in [24,25], the modal filters' concept as well as feature extraction is recalled in the present section. The extension of modal filters to automated damage localization is then explained.

2.1. Data reduction using spatial filters and modal filters

Consider a structure equipped with a network of n sensors y_k and excited with a force f as depicted in Fig. 1. The modal expansion of the frequency response function (FRF) of the response on sensor k (considering N mode shapes) is given by

$$Y_k(\omega) = \sum_{i=1}^{N} \frac{c_{ki}b_i}{(\omega_i^2 - \omega^2 + 2j\xi_i\omega_i\omega)}, \tag{1}$$

where c_{ki} is the modal output gain of sensor k, b_i is the modal input gain, ω_i is the ith angular natural frequency and ξ_i is the modal damping of mode i. When the number of sensors is very large, it is interesting to perform data reduction in order to decrease the power consumption and the bandwidth needed to transmit the data, as well as to facilitate the data storage and post-processing. For SHM applications, an optimal reduction is one that significantly reduces the amount of data while keeping most of the information about the damage. A simple data reduction technique is spatial filtering [25]. The basic principle is illustrated in Fig. 1.

It consists in condensing the data from a network of n sensors through a linear combination to form a single output response:

$$g(t) = \sum_{k=1}^{n} \alpha_k y_k(t) \tag{2}$$

The corresponding FRF is

$$G(\omega) = \sum_{k=1}^{n} \alpha_k Y_k(\omega) = \sum_{i=1}^{N} \frac{\{\sum_{k=1}^{n} \alpha_k c_{ki}\}b_i}{(\omega_i^2 - \omega^2 + 2j\xi_i\omega_i\omega)} \tag{3}$$

The idea behind modal filtering is to choose the coefficients of the linear combiner α_k in such a way that they are orthogonal to all the modes of the structure in a frequency band of interest, except mode l [35,23]:

$$\sum_{k=1}^{n} \alpha_k c_{ki} = \delta_{li}, \tag{4}$$

or in a matrix form:

$$[C]^T\{\alpha\} = \{e_l\}, \tag{5}$$

where $\{\alpha\} = \{\alpha_1 \ldots \alpha_n\}^T$ and $\{e_l\} = \{0\ 0 \ldots 1 \ldots 0\ 0\}^T$ (all components set to 0 except the lth component). The modal filter can be tuned to any of the N mode shapes of the structure. Once the modal filter coefficients α_k are defined, the linear combination is performed in the time domain. In the frequency domain, the FRF of the modal filter tuned on mode l is given by

$$G(\omega) = \frac{b_l}{(\omega_l^2 - \omega^2 + 2j\xi_l\omega_l\omega)} \tag{6}$$

Note that because the modal filtering principle is based on Eq. (4), it is still applicable if the output sensors are velocities or accelerations.

2.2. Effect of damage and environment on modal filters

Suppose now that a structural change occurs. This will change the filtered frequency response $G(\omega)$ as follows:

$$G^*(\omega) = \sum_{k=1}^{n} \alpha_k Y_k^*(\omega) = \sum_{i=1}^{N} \frac{\{\sum_{k=1}^{n} \alpha_k c_{ki}^*\}b_i^*}{(\omega_i^{*2} - \omega^2 + 2j\xi_i^*\omega_i^*\omega)}, \tag{7}$$

where * refers to the properties of the modified structure. The structural change will affect the following quantities:

(i) b_i^*: change of the modal input gain.
(ii) ω_i^* and ξ_i^*: changes of the eigenfrequencies and the modal damping.
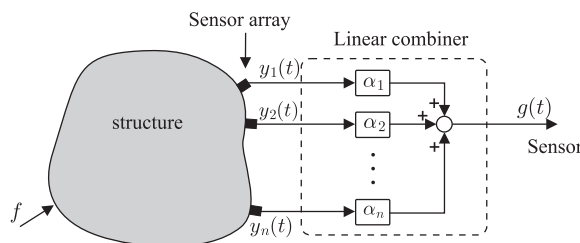

Fig. 1. Principle of spatial filtering on a network of n sensors.

(iii) c_{ki}^*: change of the mode shapes. Depending on the nature of the mode shape change, the effect on the modal filter differs. If the mode shape change is local, Eq. (4) is not satisfied anymore:

$$\sum_{k=1}^{n} \alpha_k c_{ki}^* \neq \delta_{li} \tag{8}$$

In that case, the modal filter does not perfectly work and the filtered peaks will strongly reappear around eigenfrequencies ω_i with $i \neq l$ (see Fig. 2 (a)). On the other hand, for global changes of the mode shapes, the appearance of peaks is much less pronounced. In particular, for a proportional change of the stiffness or mass matrix, only the eigenfrequencies are affected, without any change in the shape of the mode shapes, so that one gets:

$$\sum_{k=1}^{n} \alpha_k c_{ki}^* = \sum_{k=1}^{n} \alpha_k \lambda c_{ki} = \lambda \delta_{li} \tag{9}$$

As a result, only the eigenfrequency of the modal filter is affected (Fig. 2(b)).

In practice, the linear combiner coefficients α_k should be computed using experimentally identified mode shapes in order to avoid the need to build a numerical model. This can be achieved based on output-only measurements, using for instance stochastic subspace based methods [12,36,13]. Note that once the α_k coefficients are known, the modal filters are implemented directly in the time domain using Eq. (2), so that the excitation does not need to be measured.

The reduction of data with modal filters has already been studied numerically in [25,26] and experimentally in [28] for damage detection. Section 2.4 details the extension of that idea to damage localization.

2.3. Signal processing for modal filter outputs

If the input force $f(t)$ is known, one can directly compute the FRF of the output of the modal filter $g(t)$ using well-established methods for FRF estimation. For random signals, the FRF is typically estimated using the ratio of the power spectra and the cross power spectra. Using the H_1 FRF estimator, the estimation of $G(\omega)$ is given by [37]

$$G(\omega) = \frac{S_{gg}(\omega)}{S_{gf}(\omega)}, \tag{10}$$

where $S_{gg}(\omega)$ is the auto-spectral density (or power spectral density – PSD) of the filtered frequency response $g(t)$ and $S_{gf}(\omega)$ is the cross-spectral density of $g(t)$ and the input $f(t)$. These power spectra can be estimated efficiently thanks to Welch's method [38]. If the input force is not known, one can simply compute the power spectral density of $g(t)$. This quantity is directly related to the amplitude of $G(\omega)$ as follows [37]:

$$S_{gg}(\omega) = |G(\omega)|^2 S_{ff}(\omega) \tag{11}$$

This relationship shows that if peaks appear in $|G(\omega)|$, they will also appear in $S_{gg}(\omega)$. On the other hand, if sharp peaks are present in the auto-spectral density of the input $S_{ff}(\omega)$, they might be interpreted as damage. In practice however, for ambient excitations in civil engineering applications, such peaks are rarely present in the excitation signal. In addition, if the frequencies corresponding to those peaks are not in the frequency bands around the natural frequencies of interest of the system, they can easily be differentiated from peaks appearing due to damage.

In summary, for output-only measurements, it is necessary to detect the appearance of peaks around the natural frequencies of the healthy system in the PSD of $g(t)$. If the input force is known, the same should be applied to the amplitude of the FRF $|G(\omega)|$, since these two quantities are closely related.
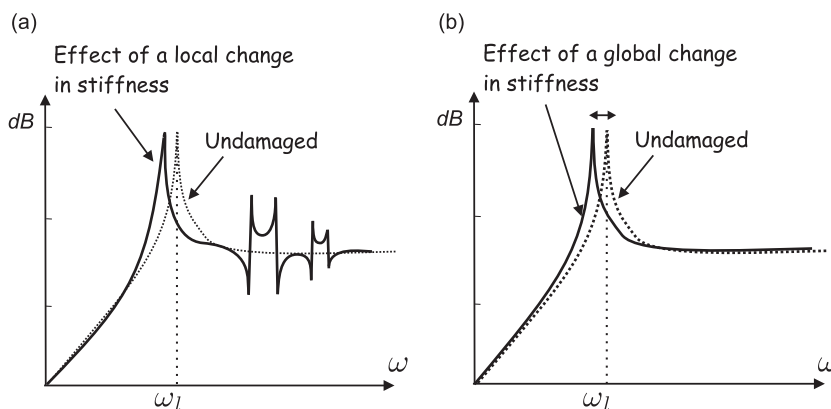

Fig. 2. Effect of a structural change on the modal filter tuned on mode l. (a) Effect of a local stiffness change, (b) effect of a global proportional stiffness change.

2.4. Extension to damage localization

The previous idea can be extended to damage localization. Consider now that the n sensors installed on the structure are grouped in several smaller sensor networks, each consisting of m sensors. Modal filters can be built for each of these local sensor networks resulting in independent *local modal filters* (see Fig. 3).

If the local network I contains sensors $y_{1,I}, \ldots, y_{m,I}$, the output of its modal filter tuned to mode l is given by

$$g_I(t) = \sum_{k=1}^{m} \alpha_{k,I} y_{k,I}(t), \tag{12}$$

where the $\alpha_{k,I}$ coefficients are computed in order to satisfy the following condition:

$$\sum_{k=1}^{m} \alpha_{k,I} c_{(k,I)i} = \delta_{li}, \tag{13}$$

where $c_{(k,I)i}$ is the kth ($k = 1, \ldots, m$) component of the ith mode shape projected on the Ith local sensor network. If a damage occurs under spatial filter I and if the sensor responses are locally sensitive to damage, the mode shape will only be altered in that spatial filter. As a result, only the spatial filter I will have spurious peaks, indicating the location of the damage. The efficiency of the approach relies therefore on a very strong assumption: damage in a local filter will cause a local change of the mode shape which is limited to the very close vicinity of the damage location. Such a property depends on the type of measured quantity which is considered. Earlier studies [30] have shown that in beam-like structures, curvatures exhibit such a property for the first low order mode shapes. A more general discussion has been made in [31], where it was demonstrated that the result can be generalized to any kind of structure using strains instead of curvatures. The importance of using mode shapes with a wavelength much larger than the size of damage was also emphasized. This has been the primary motivation for using strain measurements in several previous works [39,40]. Note however that a similar approach has been proposed in [29] using accelerations. Practical issues dealing with the computation of the modal filter coefficients for an efficient filtering are detailed in [22].

2.5. Feature extraction based on modal filter outputs

Because the spurious peaks are expected to appear around the initial eigenfrequencies of the structure, the strategy consists in extracting one feature in each frequency band around them. In previous studies, we used a feature called the peak indicator [22,41], but recent works have pointed out that it presents two major drawbacks which are (i) it does not grow monotonically with damage and (ii) it saturates quickly for low levels of damage. This is the motivation to introduce a new feature here. Consider the amplitudes of the undamaged and damaged filtered frequency responses (PSDs) $s(\omega)$ and $s^*(\omega)$ of Fig. 4.

This figure shows that for a modal filter tuned on the eigenfrequency between ω_c and ω_d, the spurious peak grows around the eigenfrequency between ω_a and ω_b. While there is also a shift of the static component of the filtered frequency response and a slight change of the amplitude of the third peak, the peak on which the modal filter is tuned remains almost unchanged when the damage increases. For this reason, the quantity $\tilde{s}_{|[\omega_a,\omega_b]}(\omega)$:

$$\tilde{s}_{|[\omega_a,\omega_b]}(\omega) = \frac{s_{|[\omega_a,\omega_b]}(\omega)}{\int_{\omega_c}^{\omega_d} s(\omega)\, d\omega} \tag{14}$$

is interesting in the sense that it is not affected by a change of the level of excitation and that it is sensitive to a change of $s(\omega)$ in the frequency band $[\omega_a, \omega_b]$. In practice, since the signals are acquired at discrete time intervals, $s(\omega)$ is obtained at discrete frequency points, so that Eq. (14) will be computed using a trapezoidal rule as follows (the dependency of s with ω
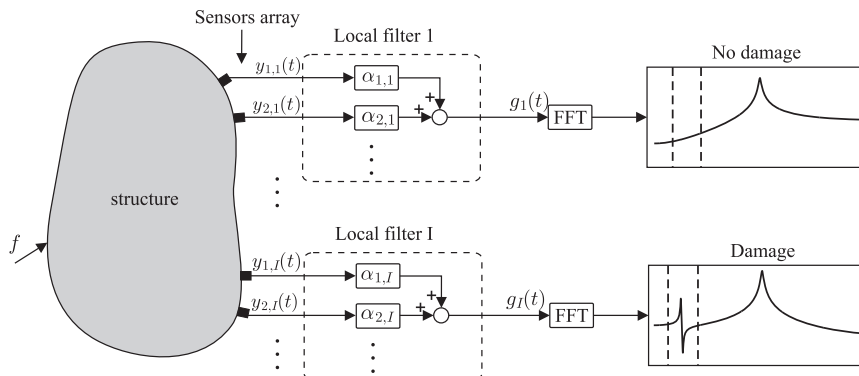

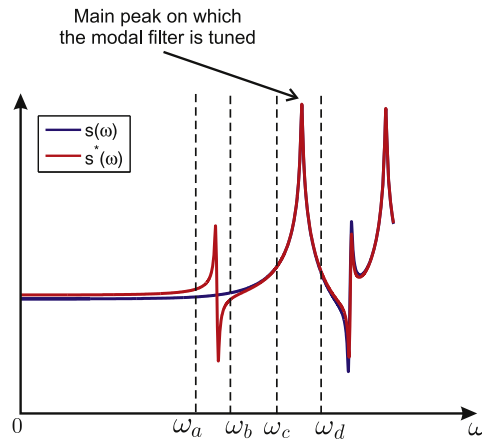**Fig. 3.** Principle of damage localization using local filters.

Fig. 4. Detection of a spurious peak based on $s(\omega)$.

is omitted in order to simplify the notations):

$$\tilde{s}_i = \frac{s_i}{\frac{\Delta\omega}{2}\sum_{j=j_c}^{j_d-1}(s_j+s_{j+1})},$$
(15)

where $s_i = s_{i_a}, \ldots, s_{i_b}$ are the n_1 discrete amplitudes of the filtered frequency response between ω_a and ω_b, $s_j = s_{j_c}, \ldots, s_{j_d}$ are the n_2 discrete amplitudes of the filtered frequency response between ω_c and ω_d, and $\Delta\omega$ is the frequency resolution. Based on the normalized frequency response of the output of the modal filter, a novel feature is defined by considering that the n_1 values of $\tilde{s}$ between ω_a and ω_b are samples of a random variable and estimating the moment of order 4 of its distribution given by

$$\tilde{m}_4 = \frac{1}{n_1}\sum_{i=i_a}^{i_b}(\tilde{s}_i - \bar{\bar{s}})^4,$$
(16)

where $\bar{\bar{s}}$ is the mean value of $\tilde{s}_i$ in the frequency band $[\omega_a, \omega_b]$. This choice is not motivated by a statistical approach, but rather by the observation that this feature is very sensitive to the growth of a peak between ω_a and ω_b which results in a change of the sharpness of the distribution of the samples that is well reflected by the moment of order 4. Note that while the kurtosis $\kappa = \tilde{m}_4/\sigma^4$ (where σ stands for the standard deviation of $\tilde{m}_4$) is typically used with time domain signals for damage assessment in rotating machinery [42–44], $\tilde{m}_4$ is computed here with frequency domain responses. In order to increase the sensitivity of $\tilde{m}_4$ to small damage, the feature used in the control charts will be given by $\sqrt[8]{\tilde{m}_4}$ instead of $\tilde{m}_4$. Working with $\sqrt[8]{\tilde{m}_4}$ is also more convenient because this feature is many orders of magnitudes larger than $\tilde{m}_4$. Besides its robustness with respect to a change of the level of excitation as already explained, another very interesting property of this damage sensitive feature is that it increases monotonically with the size of the spurious peak, and therefore with the level of the damage. This property has been demonstrated numerically in [45].

2.6. Automation of the damage localization process

In order to have an efficient damage localization method applicable to civil engineering structures, there is a need for a very simple but robust way to automatically set off alarms when damage occurs. When the excitations are random, the damage sensitive feature $\tilde{m}_4$ behaves like a random variable. That feature will therefore follow a statistical distribution which can be inferred from several undamaged samples. Many tools have been developed to detect a change in that statistical distribution such as outliers analysis or hypothesis testing. In this work, we apply the control charts [33,34]. This tool of statistical quality control plots the features or quantities representative of their statistical distribution as a function of the samples. Different univariate or multivariate control charts exist but all these control charts are based on the same principle which is summarized in Fig. 5.

In phase I, a set of samples is collected and analyzed to infer statistical characteristics of the process when it is assumed to be in control (i.e. when the structure is undamaged). The aim of this step is to compute the control limits (upper control limit UCL and/or lower control limits LCL) between which the feature should be included if the process stays in control. Those limits are governed by the statistical distribution $f(x)$ of the quality characteristic and the probability $1-\gamma$ that any in-control sample will fall inside the control limits. There are control limits that can be computed to detect a shift of the mean value of the process or a shift of the variance of the process.

Once a set of reliable control charts has been established (phase I), the process is under monitoring (phase II). The process state is unknown (it might be in or out of control), and if a sample falls outside the control limits previously computed, it is considered as an abnormal value, and a warning is triggered. An alarm will only be set off if the proportion of warnings for a given number of
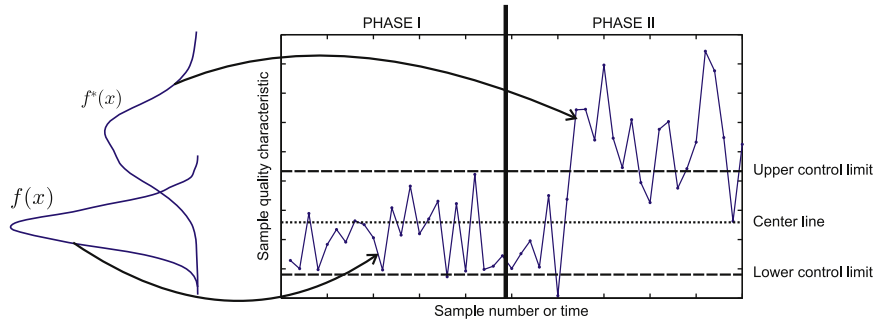
Fig. 5. A typical control chart.

samples exceeds γ considered to compute the control limits. This will be typically the case if the features are described by a new probability density function $f^*(x)$ due to a change of the process. To avoid too frequent false alarms, an arbitrary proportion γ^* bigger than γ can be chosen to release alarms. The phase I fixes the probability of type I (false alarms) and type II (missing alarms) errors. Because the control limits values are based on the number of samples in the in-control set of data, the statistical distribution $f(x)$ and the γ value, the statistical analysis must be done very carefully.

Typically, one can find two families of control charts in the literature: the univariate control charts and the multivariate control charts. The first family will be used if there is only one feature to be monitored while the second one is used when several features are monitored at the same time. In our application, this means that if we check the appearance of only one spurious peak around one given natural frequency in each local filter, we will apply the univariate control chart on that feature while we will use a multivariate control chart if we check the spurious peaks around several eigenfrequencies in each spatial filter. Finally, there are two categories of control charts in each family: the Shewart control chart and the time weighted control charts. The first category monitors each sample independently while the second category considers the previous samples to monitor the current sample, which allows us to detect smaller shifts. It has been found that the best results are obtained when the Shewart control charts are applied, because the time weighted control charts increased too much the number of type I errors. We will therefore only present the univariate and the Hotelling T^2 control charts. For other control charts, the interested reader should refer to the excellent books [33,34].

Individual control chart: Consider that only one feature x following a normal distribution is monitored (one $\tilde{m}_4$ value in each spatial filter for example). The individual control chart will monitor that individual feature x. The control limits are

$$\textit{Upper Control Limit}: \ UCL = \overline{x} + 3\frac{\overline{MR}}{d_2}$$

$$\textit{Lower Control Limit}: \ LCL = \overline{x} - 3\frac{\overline{MR}}{d_2} \tag{17}$$

If the number of samples in phase I is n, then:

$$\overline{x} = \frac{1}{n}\sum_{i=1}^{n} x_i, \tag{18}$$

$$\overline{MR} = \frac{1}{n}\sum_{i=2}^{n} |x_i - x_{i-1}|, \tag{19}$$

and $d_2 = 1.128$. In fact, $\overline{MR}/d_2$ is an estimate of the standard deviation σ of x (assumed to follow a normal distribution) in phase I. Eq. (17) is therefore based on a choice of $\gamma = 0.027$. The individual control chart is designed to detect a shift of $\overline{x}$.

Hotelling T^2 control chart: If two or more features are monitored at the same time, monitoring these two quantities independently by applying two or more univariate control charts can be very misleading, especially if those features are correlated. On the opposite, the Hotelling T^2 control chart is designed for the monitoring of several features simultaneously. Consider p features following a p-normal distribution. The Hotelling T^2 control chart monitors the Mahalanobis distance T^2:

$$T^2 = (x - \overline{x})^T \Sigma^{-1} (x - \overline{x}), \tag{20}$$

where Σ is the $p \times p$ estimated covariance matrix of features, x is the current $p \times 1$ feature vector, and $\overline{x}$ is the $p \times 1$ vector of estimated mean values of x vectors (only the undamaged samples are considered to obtain Σ and $\overline{x}$). Since the Mahalanobis distance is always positive, only the upper control limit UCL is based on a F distribution:

$$UCL = \frac{p(m+1)(m-1)}{(m^2 - mp)} F_{\gamma, p, m-p}, \tag{21}$$

where p is the number of variables, m is the number of samples in the set of data in phase I, and γ is such that there is a probability of $1 - \gamma$ that any in control sample will fall between the control limits. Like the individual control chart, the Hotelling T^2 control chart detects a change of $\overline{x}$.

2.7. Summary of the proposed method

Fig. 6 summarizes the application of the automated damage localization using local modal filters:
The successive steps are

(A) Initialization of the monitoring system: the structure is assumed to be undamaged and this phase needs a very basic user interaction.
1. Identify the mode shapes as well as the corresponding eigenfrequencies in the bandwidth of interest.
2. Choose and compute the modal filter coefficients for each local sensor network (i.e. compute the coefficients $\alpha_{k,l}$ from Eq. (13)).
3. Extract a set of samples of the feature vector for the undamaged structure:
   (i) Measure the responses $g_l(t)$ of each local modal filter (real time linear combination of sensor responses) for a given acquisition time.
   (ii) Compute the PSD $S_{l,gg}(\omega)$ of each $g_l(t)$.
   (iii) Extract the damage sensitive feature $\tilde{m}_4$ from each PSD.
4. Compute the control limits based on the features ($\tilde{m}_4$ here) collected for several undamaged samples to apply the control charts.
(B) From here, the system is ready for the monitoring: there is no more user interaction and the structure state is unknown. The data processing is carried out in each local sensors network independently:
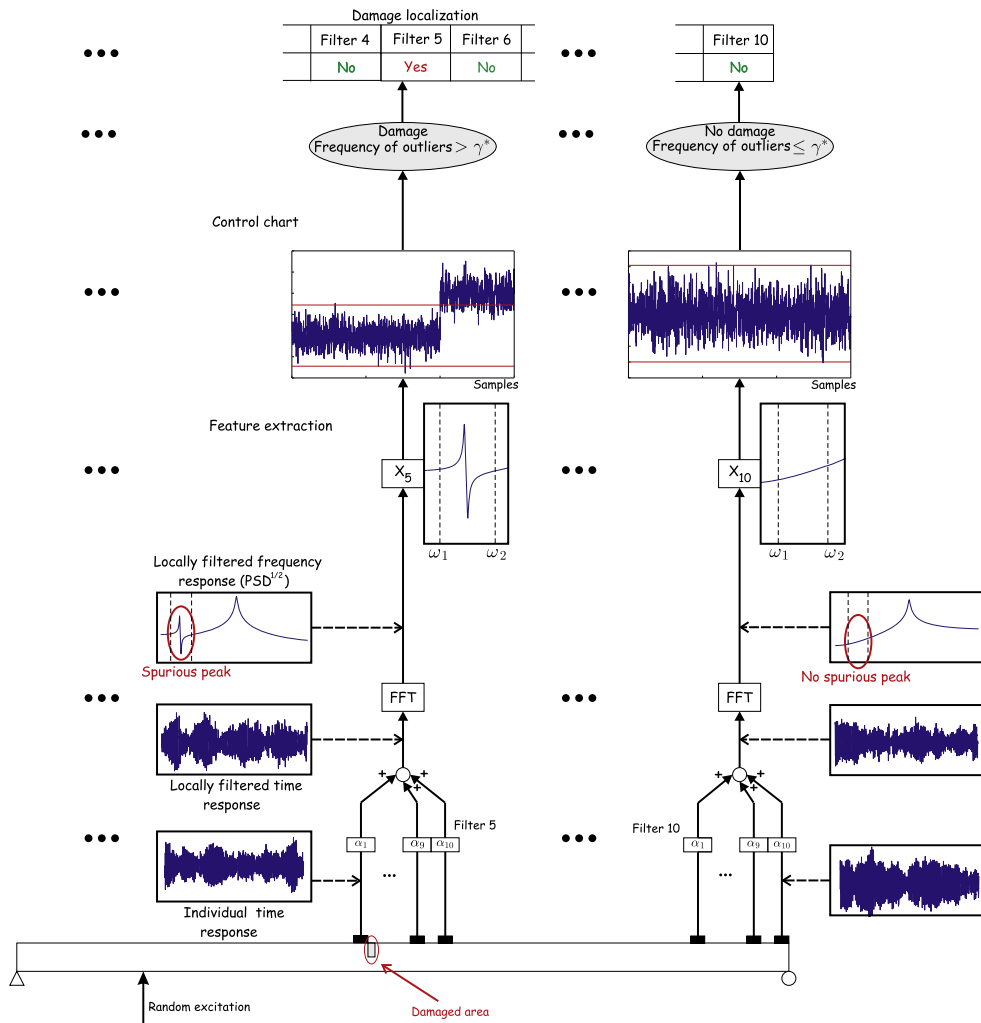1. Extract the features:
   (i) Measure the responses $g_l(t)$.

Fig. 6. Flow chart of damage localization using local modal filters.

(ii) Compute $S_{I,gg}(\omega)$.
(iii) Compute the moment of order 4 $\tilde{m}_4$.

2. Check if the feature vector composed of the $\tilde{m}_4$ values of interest falls inside the control limits.

If the frequency of alarms exceeds the threshold γ^*, the damage is detected and assumed to be located in the area covered by the local network. The main advantages of the proposed method are

(i) Its low computational cost and applicability to any kind of structure.
(ii) The possibility to use in-service ambient vibrations.
(iii) The full automation of the process, once the initialization phase has been done.
(iv) The fact that it is a data-based (no physical model needed) and unsupervised (no need for training data from the damaged structure) method.

3. Experimental case studies

3.1. Clamped-free steel plate

3.1.1. Description of the case study

Fig. 7 shows an overview of the first experimental setup [46] which is investigated. The structure consists of a 100 mm × 670 mm × 3 mm clamped-free steel plate. One PZT actuator is used to excite the structure, and eight 13 mm × 60 mm × 50 µm low-cost (around 4€/piece) PVDFs sensors from *Measurement Specialties*™ (DT Series Lead attachments [47]) are used to measure dynamic strains. These sensors are numbered from the clamped edge of the plate and cover continuously the structure along its length. A National Instrument PXIe-1082 data acquisition system is used to measure the eight voltages from the PVDFs at the same time. The PZT actuator is driven with a band-limited white noise between 0 Hz and 50 Hz (not measured) generated by the PXI, and powered by a MIDE voltage amplifier. In all cases, the measurements last for 30 s and the sampling frequency is 1600 Hz. Several threaded holes are drilled all along the plate,

(a)

(b)

Actuator (PZT)

Sensor

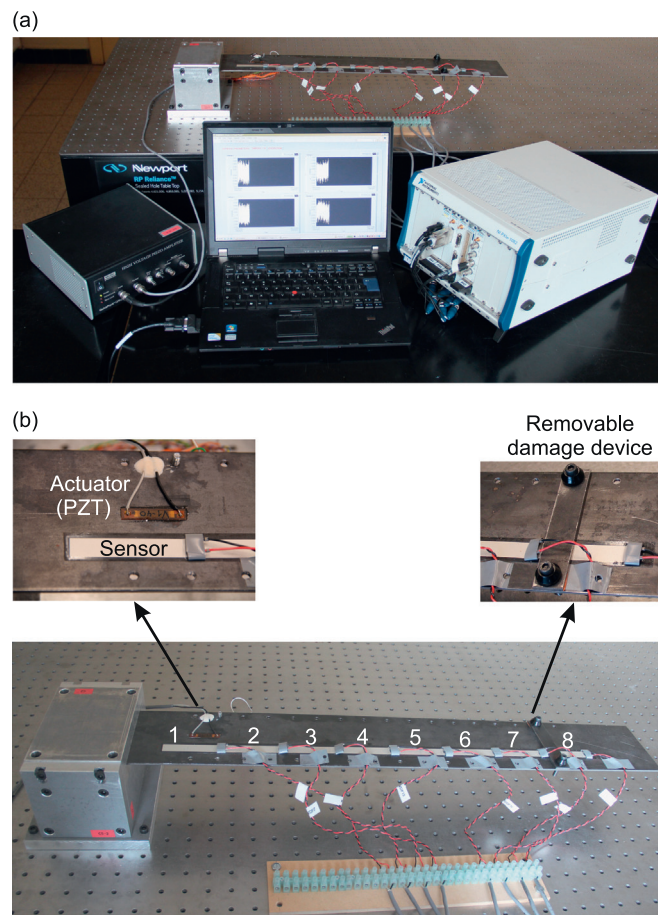Removable damage device

1 2 3 4 5 6 7 8

Fig. 7. Experimental setup. (a) Overall view of the experimental setup, (b) detailed view of the instrumented structure.

so that a 100 mm × 20 mm × 3 mm small removable damage device can be fixed over any sensor in order to produce a local structural change that will be considered as a representative of damage.

Because of the limited number of sensors, it has been chosen to consider 3 local filters of 4 sensors, with an overlap of two sensors: sensors 1–4, 3–6 and 5–8. Note that the idea of overlapping the local filters has been previously applied by Mendrok and Uhl in [29]. The main differences with the application of local modal filters in the present paper are that we use strain measurements instead of accelerations, and that the filtered frequency responses are based on output-only measurements while Mendrok and Uhl apply modal filters on FRFs which require input–output measurements. We will investigate the damage scenarios given in Table 1, which also gives the local filters covering the damage.

3.1.2. Undamaged structure

Using the stochastic subspace identification method [12] implemented in the *Macec Toolbox* in *Matlab*, we have been able to identify correctly the two first undamaged bending mode shapes Φ_1 ($f_1 = 5.27$ Hz) and Φ_2 ($f_2 = 32.51$ Hz). Since it has been demonstrated in several numerical and experimental studies that the effect of a damage is more local for low order mode shapes, it has been chosen to only consider modal filters tuned on Φ_2 and to check the appearance of spurious peaks around f_1 for each local filter.

3.1.3. Removable damage device

In order to simulate experimentally a damage, we have designed a small device which we call a "*removable damage device*" (see Fig. 7(b)) shortened in RDD. The primary aim of this device is to produce a local change of the strains on the mode shapes in order to test our damage localization method. It consists of a small plate which can be fixed with two bolts at different locations along the length of the clamped-free plate. The structure with or without removable damage device could be considered as the undamaged (reference) structure, but it was found preferable to take into account the structure without removable damage device for the baseline. This is due to the fact that the torque applied to the screws to fix the panel is not easily repeatable, which could cause variations in the baseline condition [28]. The purpose of the removable damage device is therefore to check if the method succeeds to locate an arbitrary local change of strains. If it does, the next step is to compare the results with the damage localization of a real damage, which is one of the perspectives of the present work.

A numerical model of the clamped-free steel plate has also been built using the *Structural Dynamic Toolbox* in *Matlab* [48], and is shown in Fig. 8. In this model made of 670 Euler–Bernoulli beam elements, the same dimensions than the experimental setup are considered, and the RDD is modeled as a local change of stiffness $\Delta K = 5$ percent and a local change of mass $\Delta M = 100$ percent at the same positions than in the experimental tests. Note that while the change of mass due to the RDD is known precisely, it is difficult to assess correctly the change of stiffness. Indeed, it is not possible to have an infinitely rigid connection of the RDD to the host structure. Finally, the numerical strains are considered along 8 strain sensors with very similar sizes and positions than the PVDFs sensors.

Fig. 9 displays the evolution of the first and second eigenfrequencies when the local change of stiffness and mass occurs at sensors 2–8 (the eigenfrequencies with a local structural change $f_{i,RDD}$ are normalized with respect to the undamaged eigenfrequency f_i, with $i = 1,2$). The absolute difference $|\Delta(Re\Phi_i)|$ between the undamaged and damaged mode shapes is also shown for some positions of the local structural change. Because the local structural change consists of an increase of stiffness and mass, it is likely that the local effect will not be seen on the strain mode shapes when the eigenfrequency has strongly decreased. Indeed, in such a situation, the dominant effect is the mass effect which affects globally the strain mode shape. For instance, it is impossible to locate the structural change based on the change of strain mode shape when it is located at sensor 8 for the first mode (Fig. 9(a)), and when it is located on sensor 3 for the second mode (Fig. 9(b)). On the other hand, if the decrease of eigenfrequency is small or if the eigenfrequency increases, there is a chance to observe a local

Table 1
Damage scenarios.

Case	Samples	Location of damage (*sensor*)	Location of damage (*local filter*)
1	1–1000	None	None
2	1001–1250	3	[1:4] and [3:6]
3	1251–1500	4	[1:4] and [3:6]
4	1501–1750	8	[5:8]
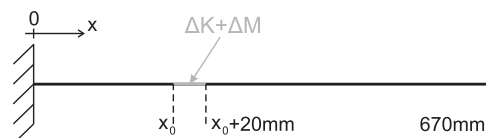
Fig. 8. Numerical model of a clamped-free plate and a damage (local change of stiffness and mass).
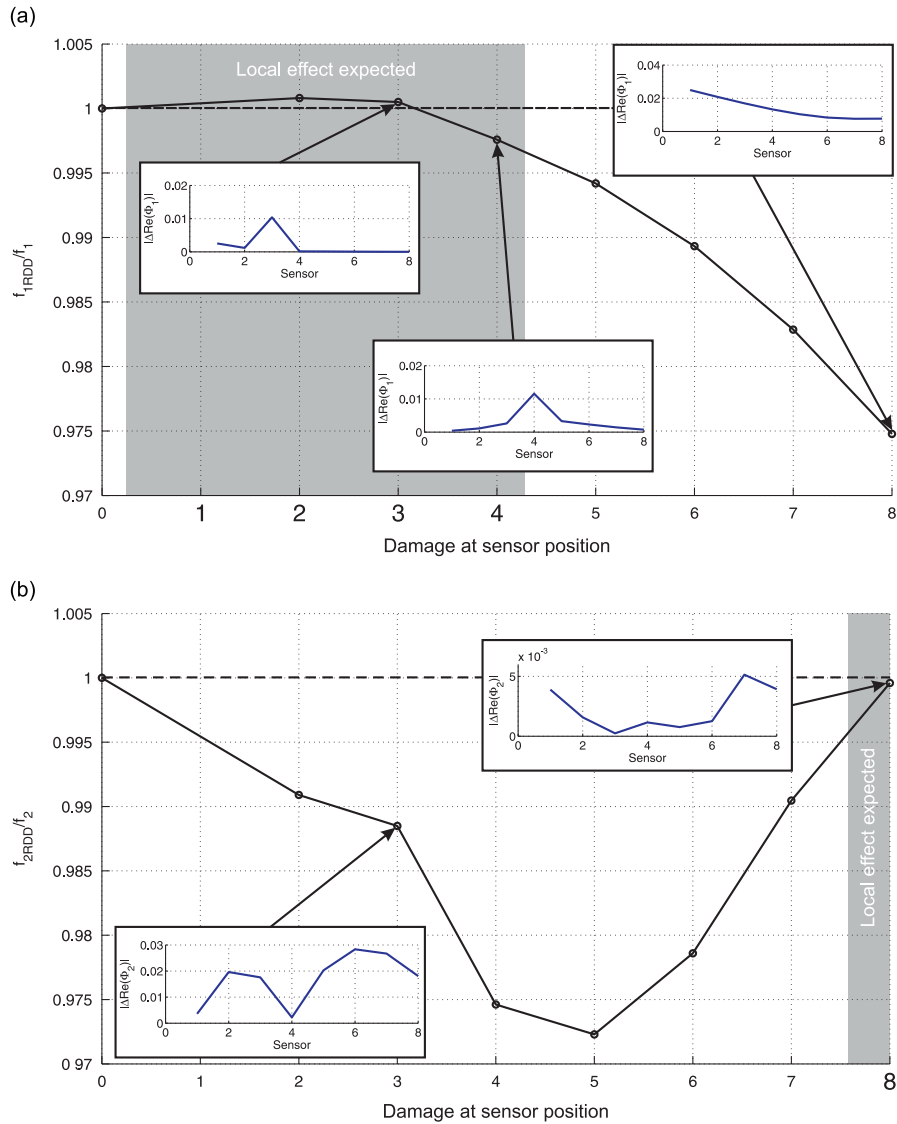
Fig. 9. Effect of a local change of stiffness and mass on eigenfrequencies. (a) First strain mode shape, (b) second strain mode shape.

effect on the change of strain mode shapes since the stiffening effect becomes strong. This is confirmed in Fig. 9(a) for a local structural change at sensors 3 and 4, or in Fig. 9(b) for a local structural change at sensor 8.

Based on these considerations, we can define the positions at which the local structural change can be considered as a representative of a damage for which a local change of strain mode shapes is observable. A local structural change seems to be representative of a damage when it is located at the first four sensors by considering the first mode and at sensor 8 with the second mode.

The same conclusions as in the numerical investigation can be drawn with the experimental setup. Fig. 10 shows the evolution of the two first eigenfrequencies when the RDD is located at sensors 2–8 (top surface).

It can be seen that the experimental changes of eigenfrequencies due to the RDD are very close to the numerical ones. Again, the change of strain mode shapes is highlighted for the same sensors than in Fig. 9, and the positions for which the RDD represents correctly a damage are the same than previously. These results justify why we have investigated a damage only at sensors 3, 4 and 8 (see Table 1), since it was not possible to fix the RDD over sensor 1 because of the PZT used for actuation (see Fig. 7(b)), and that the local effect of the RDD at sensors 2 and 3 is very similar.

It is worth mentioning that despite the fact that a local increase of 5 percent of the stiffness in the numerical model matches quite well the experimental results, it cannot be considered as the exact increase of stiffness of the RDD. An accurate estimate of the local stiffening requires more investigations, which is beyond the focus of this paper. However, considering the very small change of experimental eigenfrequencies (less than 0.5 percent), it makes sense to assume that the RDD represents a *small* damage.

The same experimental damage cases have been tested when the RDD is fixed on the bottom surface of the steel plate, opposite to the PVDF sensor. However, it turned out that in this configuration, the local effect was much smaller than when the RDD is placed on the top surface. The change of neutral axis as depicted in Fig. 11 allows us to understand this property.

At the location of the RDD, the profile of the plate becomes asymmetrical, which leads to a shift of the neutral axis as shown in Fig. 11(a). Because the strain is proportional to the distance at the neutral axis, the local change of strain is stronger when the PVDF and the RDD are placed on the same side. Indeed, in this configuration, the decrease of distance between the PVDF and the neutral axis tends to decrease the strain at the location of the PVDF. This effect accentuates the stiffening effect of the RDD, so that the strain measured by the PVDF decreases. On the other hand, the distance to the neutral axis increases if the PVDF is placed opposite to the RDD, which tends to increase the strain measured. This increase of strain is limited by
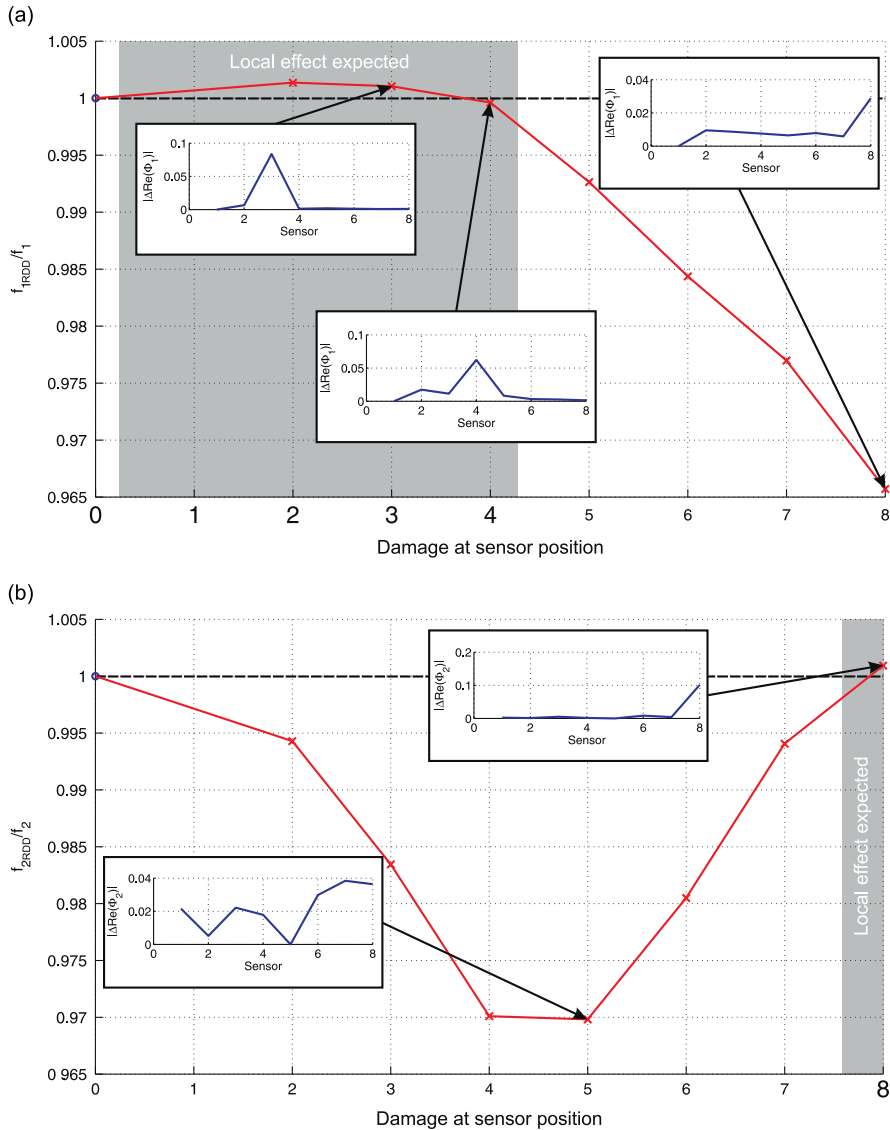
Fig. 10. Effect of RDD on eigenfrequencies: experimental measurements. (a) First strain mode shape, (b) second strain mode shape.
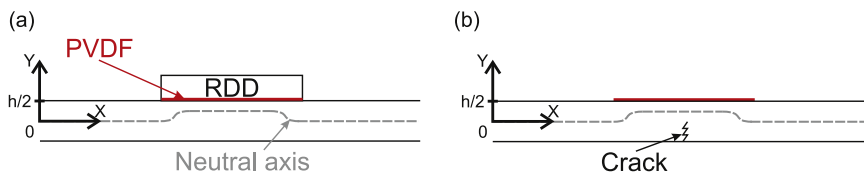

Fig. 11. Effect of local structural change on the neutral axis. (a) RDD, (b) crack.

the stiffening effect, leading to a smaller change of stiffness. It is interesting to mention that in the case of a real crack, there is also a change of the neutral axis as shown in Fig. 11(b) which will affect differently the change of strain measured by the PVDF sensor depending on its position on the plate, leading to a very similar conclusion as with the RDD. Indeed, if the PVDF is opposite to the crack, the softening at the location of the crack is countered by a decrease of the distance to the neutral axis, which limits the local change (increase) of strain. If the PVDF sensor is placed on the same side than the crack, the increase of distance to the neutral axis and the softening effect tends to increase the strain that will be measured, which enhanced the local effect that will be observed.

3.1.4. Filtered frequency response

Fig. 12 compares the filtered frequency responses of the modal filters tuned to the second eigenfrequency for local filters [1:4] and [5:8] for cases 1, 3 and 4. The frequency band in which the spurious peak is expected to appear is shown with the two vertical dashed lines. This interval $[\omega_a, \omega_b]$ and the interval $[\omega_c, \omega_d]$ used for the normalization of the amplitude of the filtered frequency response (Eq. (14)) before the computation of $\sqrt[8]{\widetilde{m}_4}$ correspond to $\omega_1 \pm 10$ percent and $\omega_2 \pm 10$ percent respectively. This choice of frequency bands is justified by the fact that we are interested in early damage localization, for which the shifts of eigenfrequencies are much smaller than the ones due to environmental effects. Because it has been observed in [49,50] that the eigenfrequencies of real bridges are typically varying within ± 10 percent around their mean value, we assume that such frequency bands are wide enough to include the spurious peaks.

As it can be seen, the peak around the first eigenfrequency is efficiently filtered. Fig. 12(a) shows clearly the possibility of locating damage with local filters. Indeed, the local filter [1:4] presents a spurious peak for damage scenario 3 (RDD over sensor 4), but not for damage scenario 4 (RDD over sensor 8). For local filter [5:8], the damage localization is more difficult. This is in particular due to the fact that the level of the sensor responses decreases at the free extremity of the plate, which tends to increase the sensitivity of the filtered frequency responses to noise.

3.1.5. Automated damage localization

In order to automate the damage localization, we apply the individual control charts on $\sqrt[8]{\widetilde{m}_4}$ for each local filter separately, since we are interested in the appearance of spurious peak around the first eigenfrequency only. The control limits are based on the first 750 undamaged samples during which the structure is assumed to be undamaged. The control limits are computed by considering a confidence interval of $\pm 3\sigma$ around the mean (undamaged) value of $\sqrt[8]{\widetilde{m}_4}$. Hence, 99.73 percent of the values of the features will fall in this interval if there is no change of the state. On the other hand, if less than 99.73 percent features fall in the confidence interval, we will assume that a damage appeared in the local filter. In practice however, considering such a high threshold leads to too many false alarms. This can be explained by the fact that

(i) Only 750 samples are used to estimate σ, so that there is an uncertainty on the estimated standard deviation, and therefore an uncertainty on the confidence levels as well.
(ii) The estimation of the percentage of in-control features is based on a finite number of samples. In this application, we group every 100 samples in one "samples set" for which we compute the percentage of in-control features. A confidence level of 99.73 percent can therefore not be used to trigger alarms as it corresponds to less than 1 sample.
(iii) There is some potential presence of "outliers" due to bad quality measurements.
(iv) The distribution of the feature to monitor is never perfectly Gaussian and usually most of the deviation is in the tails of the distribution. For high confidence levels, the tails of the distribution have a high impact.

Due to these issues, we consider in this study that the damage is located when less than 90 percent of the features in each set of 100 samples fall in the confidence interval. Figs. 13–15 summarize the application of the univariate control chart as well as the automated damaged localization.
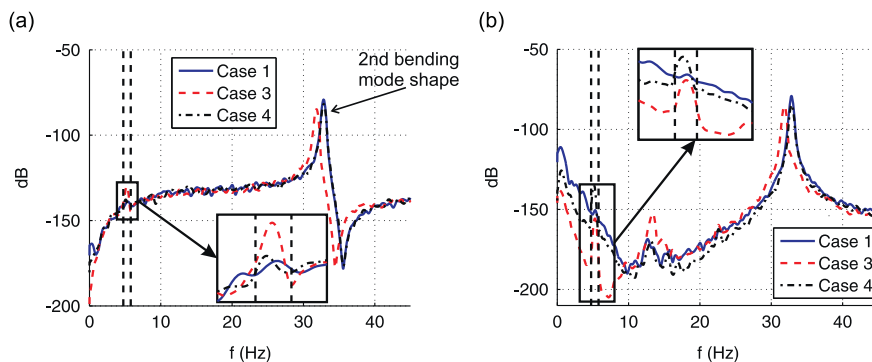

Fig. 12. Examples of undamaged and damaged filtered frequency responses. (a) Local filter (1:4), (b) local filter (5:8).

It is clear from these figures that all the damage cases have been correctly located. Indeed, all the percentages smaller than 90 percent (under the horizontal red line) correspond to the real damage location (see Table 1). The interest of overlapping the local filters is also clearly illustrated. Indeed, damage at sensor 3 is better detected in filter [3:6] than in filter [1:4], while damage at sensor 4 is better detected in filter [1:4] than in filter [3:6]. This illustrates a general property of the modal filters: it has been shown in [51] that the modal filters coefficients are very often (but not always) maximum at the edges of the filters. As a consequence, small damage at the extremities of the filters is more strongly amplified, and can therefore be detected more easily than damage located close to the center of the filter, where the modal filters' coefficients tend to zero.
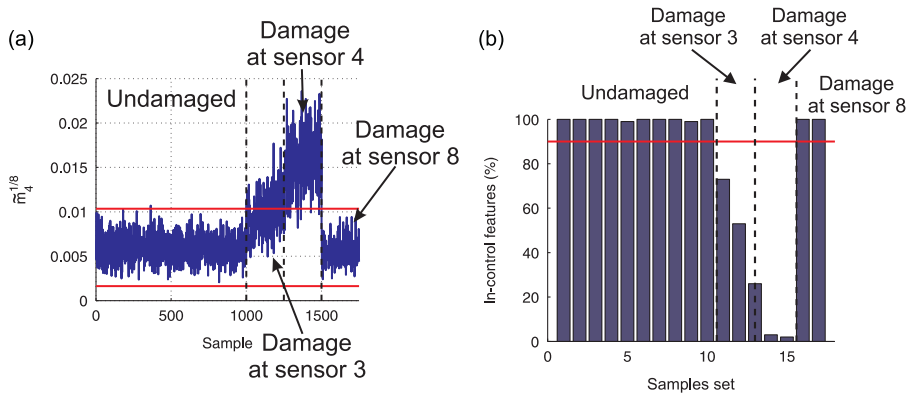
Fig. 13. Automated damage detection in local filter (1:4). (a) Individual control chart, (b) damage alarms. (For interpretation of the references to color in this figure caption, the reader is referred to the web version of this paper.)
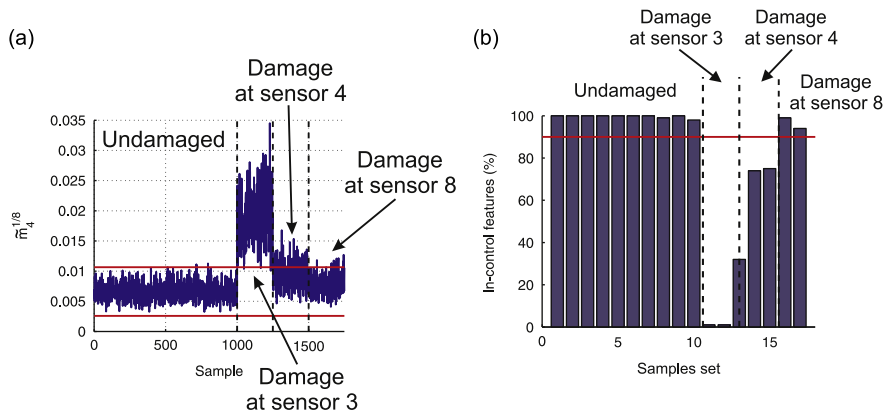
Fig. 14. Automated damage detection in local filter (3:6). (a) Individual control chart, (b) damage alarms. (For interpretation of the references to color in this figure caption, the reader is referred to the web version of this paper.)
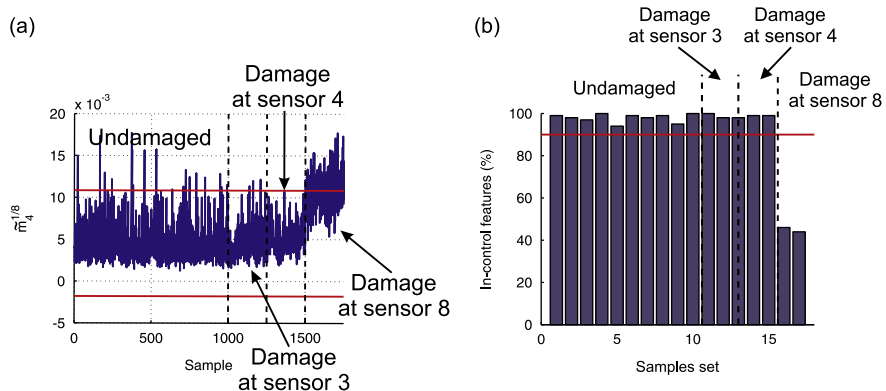
Fig. 15. Automated damage detection in local filter (5:8). (a) Individual control chart, (b) damage alarms. (For interpretation of the references to color in this figure caption, the reader is referred to the web version of this paper.)

3.2. Steel I-beam

#### 3.2.1. Description of the case study

This second experimental application consists of a 3.78 m long steel I-beam which is bolted on two big concrete cubes. The structure is excited with a Modal 110 electro-dynamic shaker from MB Dynamics, and a network of twenty 13 mm × 170 mm × 50 μm low-cost PVDFs sensors has been fixed with a double-coated tape, providing a continuous measurement of the strains along the beam between sensors 1 and 20. Since they have been installed close to the edge of the flange, these sensors are sensitive to bending, as well as to torsion of the beam. The same National Instrument PXIe-1082 data acquisition system as in the previous case study is used to measure the sensor responses with a sampling frequency of 6400 Hz, as well as to generate a band-limited white noise between 0 Hz and 500 Hz (not measured) which drives the shaker. Fig. 16 shows different views of the experimental setup as well as the definition of the PVDFs sensors. Note that the network of 36 accelerometers which was initially installed for preliminary tests can be seen, but will not be considered in the next sections.

As in the previous experimental application of modal filters to locate damage (Section 3.1), the damage is introduced by fixing a very small steel removable damage device (35 mm × 65 mm × 17 mm) with a small builder clamp directly against the PVDF sensors, as shown in Fig. 16(b). It has been chosen to consider 5 local filters of 5 sensors, with a small overlap: (i) [1:5], (ii) [4:8], (iii) [8:12], (iv) [12:16] and (v) [16:20]. The damage scenarios described in Table 2 will be investigated.

3.2.2. Undamaged structure

Preliminary forced vibration tests performed with 36 accelerometers measuring the vertical acceleration of the top flange allowed us to identify the nature of mode shapes by comparing the experimentally obtained modal parameters with the numerical modal parameters. The finite element model of the structure is made of 4-node quadrilateral plate elements using the *Structural Dynamics Toolbox* [48] under *Matlab*. Fig. 17 shows the first two bending mode shapes, while Table 3 compares the experimental and numerical eigenfrequencies and gives the *MAC* values.

The table shows that the mode shapes are in good agreement. The deviations on the eigenfrequencies are higher, as it is often the case due to uncertainties in the boundary conditions. Note however that the error on the first eigenfrequency is quite higher than could be expected. As this is not an important issue for the application of our method, the reason for this high error was not investigated.

(a)

(b)

(c)
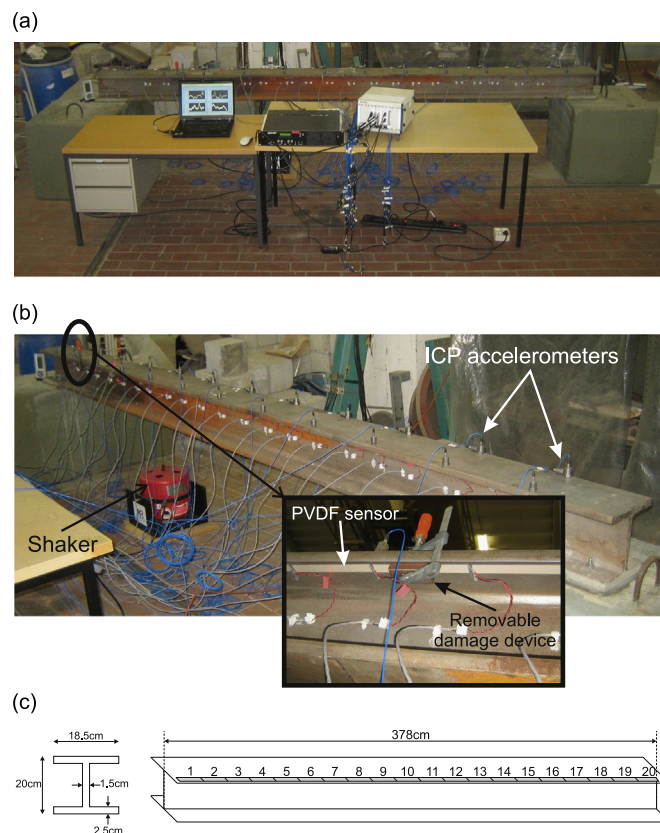
Fig. 16. Experimental setup : 3.78 m steel I-beam equipped with 20 dynamic strain sensors (PVDF) for damage localization. (a) Front view, (b) side view, (c) artist front view: definition of the PVDF sensors.

Table 2
Damage scenarios.

Case	Samples	Location of damage (sensor)	Location of damage (local filter)
1	1–300	None	None
2	301–350	1	[1:5]
3	351–400	2	[1:5]
4	401–450	3	[1:5]
5	451–500	4	[1:5] and [4:8]
6	501–550	5	[1:5] and [4:8]
7	551–600	None	None

(a)

(b)
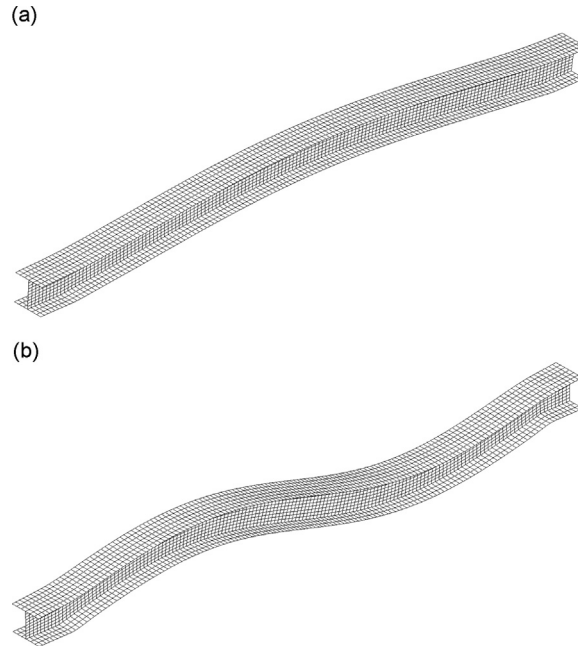
Fig. 17. Numerical bending mode shapes. (a) Mode 1 at 64.1 Hz, (b) mode 3 at 226.01 Hz.

Table 3
Comparison of the numerical and experimental modal parameters.

Mode shape	f_i (numerical, Hz)	f_i (experimental, Hz)	MAC
Mode 1 (bending)	88.49	64.1	0.97
Mode 2 (torsion)	154.6	158.11	0.94
Mode 3 (bending)	225.8	226.01	0.96

3.2.3. Damaged structure

For the different damage scenarios, the eigenfrequencies as well as the mode shapes have been identified in order to quantify the impact of the damage simulated by adding the small RDD. As it was previously observed in Section 3.1.3, the effect of the RDD on the low order strain mode shapes (real components) is local (Figs. 18 and 19) and the change of eigenfrequencies is small (Table 4):

The modal filters tuned on the two first bending mode shapes at 64 Hz and 230 Hz (see Fig. 17) have been applied for each local filter separately. Figs. 20–22 compare the filtered frequency responses of the first three local filters for cases 1, 3 and 6. The frequency bands in which the features $\sqrt[8]{\widetilde{m}_4}$ are computed (intervals $[\omega_a, \omega_b]$ and $[\omega_c, \omega_d]$ in Eq. (14)) are also shown with the vertical dashed lines. They correspond to 64 Hz ± 10 percent and 230 Hz ± 10 percent.

We can observe from Fig. 20 that the filtering of the peak is not perfect at local filter [1:5] since there are remaining sharp peaks for the undamaged case in the frequency bands in which the spurious peak is expected to appear. However, the
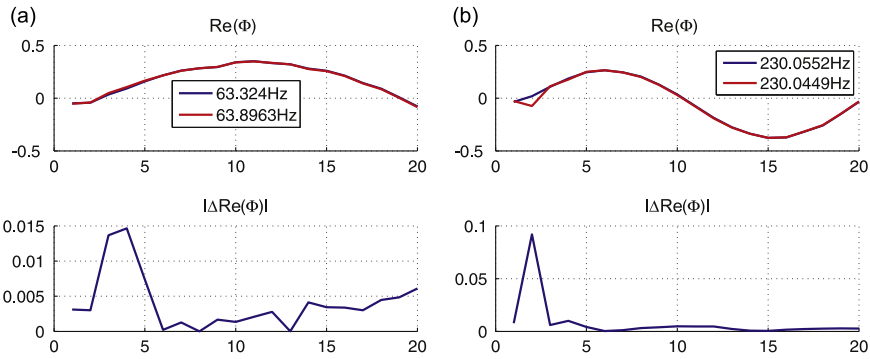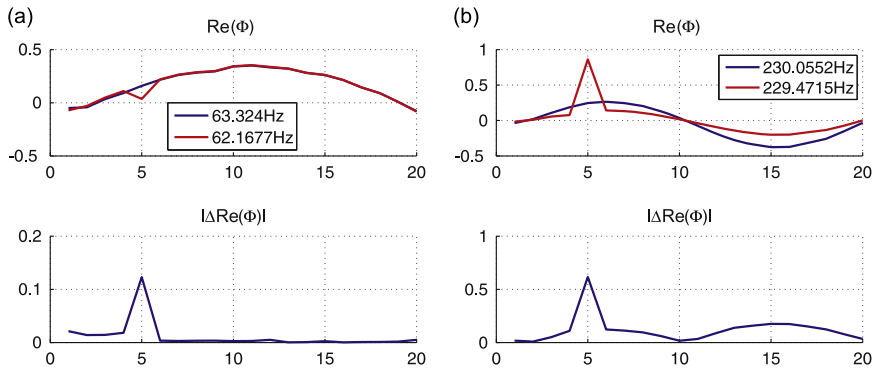
Fig. 18. RDD at sensor 2. (a) Mode 1, (b) mode 3.

Fig. 19. RDD at sensor 5. (a) Mode 1, (b) mode 3.

Table 4
Changes of eigenfrequencies due to damage.

Case	$|\Delta f_1|$ (%)	$|\Delta f_3|$ (%)
2	1.34	0.11
3	0.9	< 0.01
4	0.2	0.08
5	0.1	0.01
6	1.83	0.25

damage detection in this local filter is feasible, since the filtered frequency responses are strongly affected in the frequency bands of interest when a damage is introduced at sensors 2 (case 3) and 5 (case 6) for both modal filters.

The analysis of the filtered frequency responses at local filter [4:8] shows that the damage detection succeeds for this local filter too (Fig. 21). Indeed, there is only a clear change of the spurious peaks for damage case 6. This illustrates the possibility of damage localization: when a damage is introduced at sensor 2 (case 3), the local filter [4:8] is not affected, since it does not cover the damaged area, while when the damage is located at sensor 5, both local filters [1:5] and [4:8] react, since they both cover the damaged area.

The local sensitivity of local filters to damage is confirmed in Fig. 22: the filtered frequency responses are not affected by a damage at sensor 2 or 5.

3.2.4. Automated damage localization

Fig. 23 shows the 2D plots of the $\sqrt[8]{\tilde{m}_4}$ features computed in the intervals around 64 Hz and 230 Hz, where the appearance of spurious peaks is monitored in each local filter.

We can see from Fig. 23(a) and (b) that there is a wide variation of $\sqrt[8]{\tilde{m}_4}$ in the first interval (horizontal axis) for the undamaged samples (blue crosses), while the change of this feature in the second interval (vertical axis) is smaller. On the other hand, the $\sqrt[8]{\tilde{m}_4}$ computed around the second interval is more sensitive to the damage: the clouds related to the damage cases (red circles) can be clearly identified in the 2D plot since they correspond to a very clear shift of $\sqrt[8]{\tilde{m}_4}$ in the second interval. The interest of overlapping the local filters is illustrated once again: the first local filter [1:5] is sensitive to a damage at sensors 1, 2, 3 and 5, but not at sensor 4 (see Fig. 23(a)). However, the local filter [4:8] overlaps the first local filter at sensors 4 and 5 and reacts to a damage on these two sensors, allowing therefore to compensate the lack of sensitivity to a
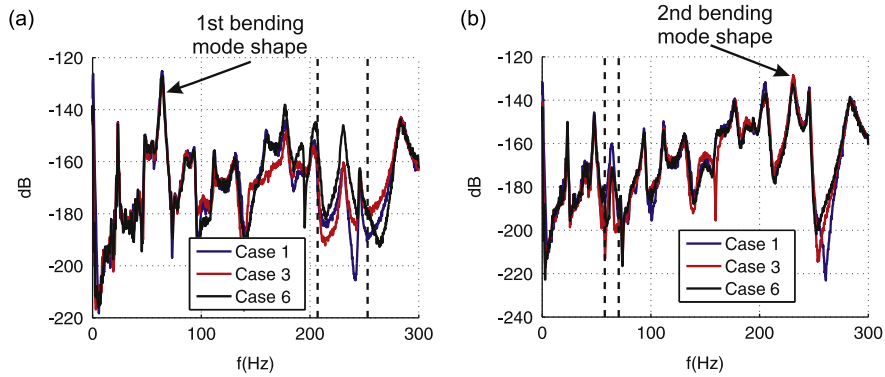
Fig. 20. Examples of undamaged and damaged filtered frequency responses for local filter (1:5). (a) Modal filter tuned on 1st bending mode, (b) modal filter tuned on 2nd bending mode.
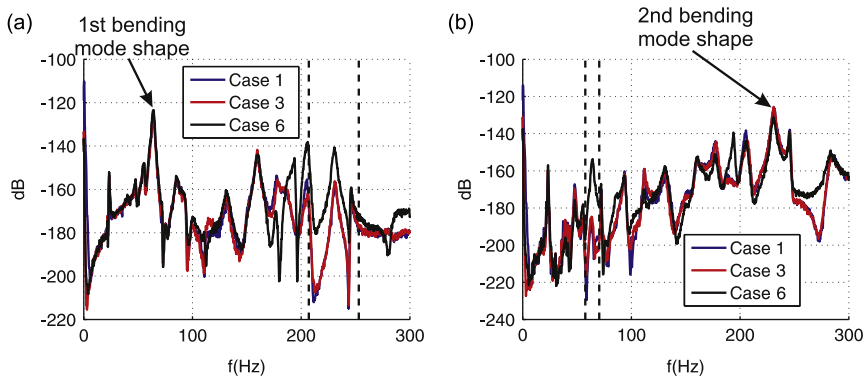

Fig. 21. Examples of undamaged and damaged filtered frequency responses for local filter (4:8). (a) Modal filter tuned on 1st bending mode, (b) modal filter tuned on 2nd bending mode.
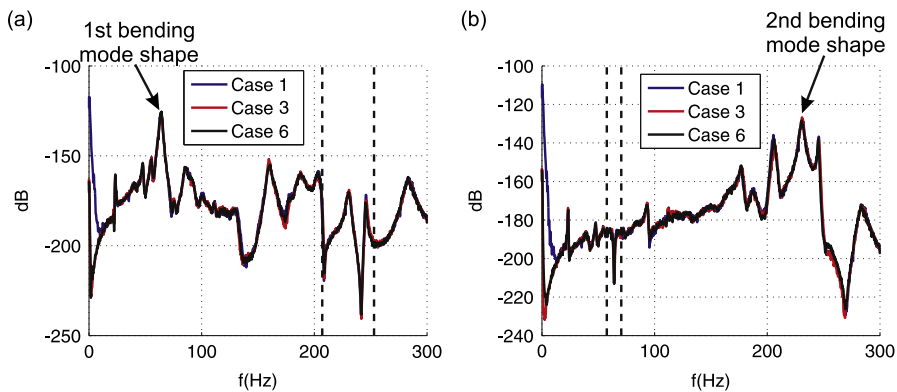

Fig. 22. Examples of undamaged and damaged filtered frequency responses for local filter (8:12). (a) Modal filter tuned on 1st bending mode, (b) modal filter tuned on 2nd bending mode.

damage at sensor 4 in the first local filter. All the other local filters do not present a clear shift of the $\sqrt[8]{\bar{m}_4}$ clouds when a damage is located in the first 5 sensors as illustrated in Fig. 23(c) for local filter [8:12].

The Hotelling T^2 control chart has been applied to automate the damage localization in each local filter. The first 200 undamaged samples have been considered to assess the covariance matrix (see Section 2.6), as well as to compute the control limit (γ is fixed to 0.25 percent). It has been observed that the first 200 undamaged features are not following closely a binormal distribution (in each local filter), which explains why γ is so small. Indeed, the Hotelling T^2 control chart is devoted to the detection of outliers from a baseline of features normally distributed as explained in Section 2.6. As a consequence, as the distribution of the features of the baseline deviates from a normal distribution, the upper control limit
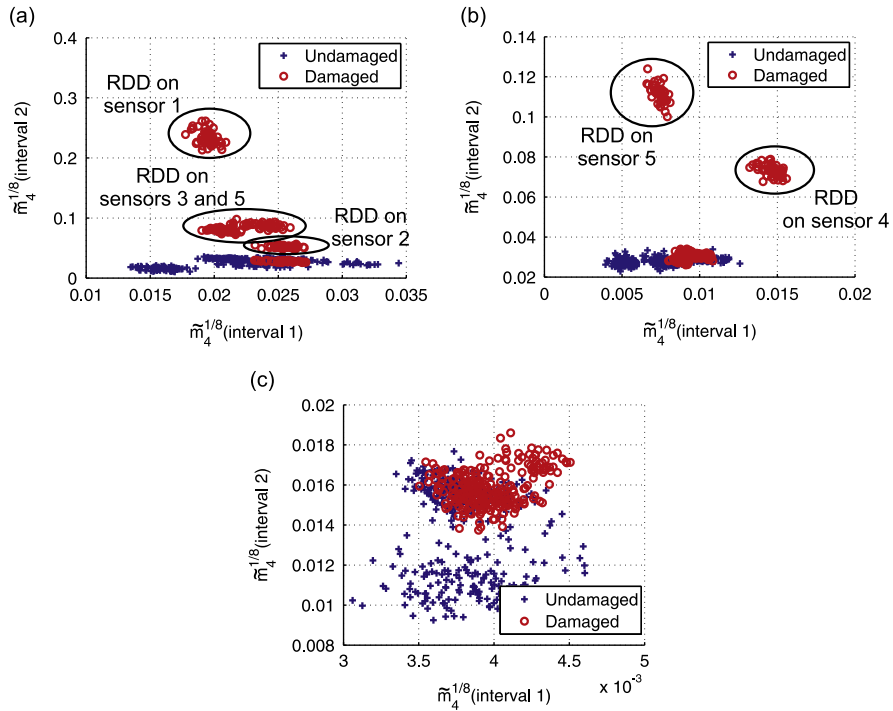
Fig. 23. 2D plot of the damage sensitive feature $\sqrt[8]{\tilde{m}_4}$. (a) Local filter (1:5), (b) local filter (4:8), (c) local filter (8:12). (For interpretation of the references to color in this figure caption, the reader is referred to the web version of this paper.)
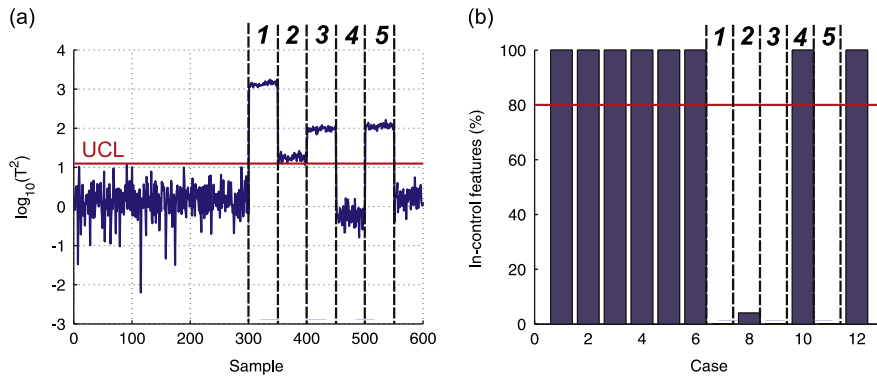

Fig. 24. Automated damage detection in local filter (1:5). (a) Hotelling T^2 control chart, (b) damage alarms.
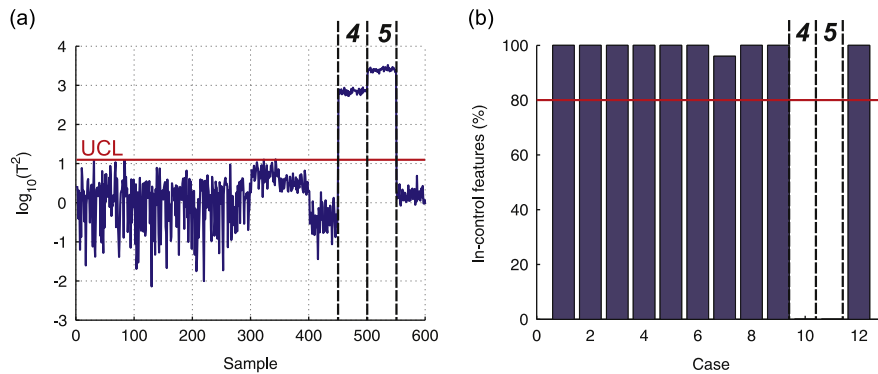

Fig. 25. Automated damage detection in local filter (4:8). (a) Hotelling T^2 control chart, (b) damage alarms.

computed with Eq. (21) becomes less adequate. For this reason, and also because we assess the percentage of in-control features every 50 samples, we consider that the damage is detected when less than 80 percent of the features fall in the confidence interval.

Figs. 24–28 summarize the application of the Hotelling T^2 control chart as well as the automated damage localization based on the criteria described previously (the position of the damage is reminded only for the local filters covering the damage). In particular, it can be seen in Figs. 24 and 25 that the increase of T^2 due to a damage is very strong (except for a damage at sensors 2 and 4 in the first local filter, see Fig. 24(a)), allowing the choice of a very small value of γ.

There is only one missing alarm in local filter [1:5] for a damage at sensor 4. However, that missing alarm is compensated thanks to the overlapping of the local filters. Indeed, the damage at sensors 4 and 5 is correctly located in local filter [4:8]. In conclusion, all the damage cases have been correctly located, and there are no false alarms: all the undamaged sample sets have more than 80 percent in-control features.
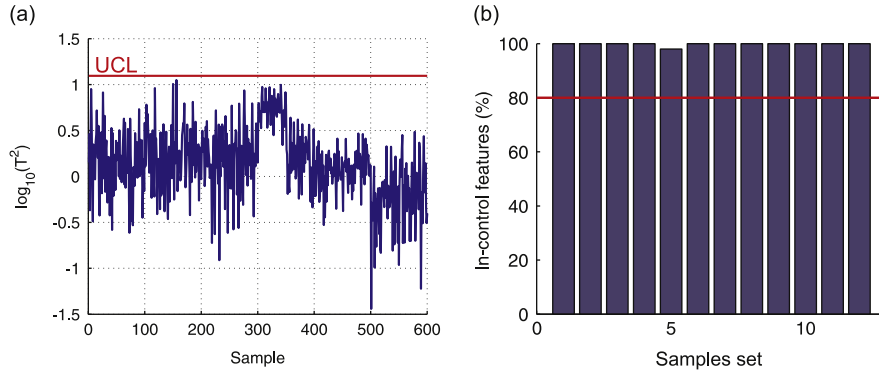

Fig. 26. Automated damage detection in local filter (8:12). (a) Hotelling T^2 control chart, (b) damage alarms.
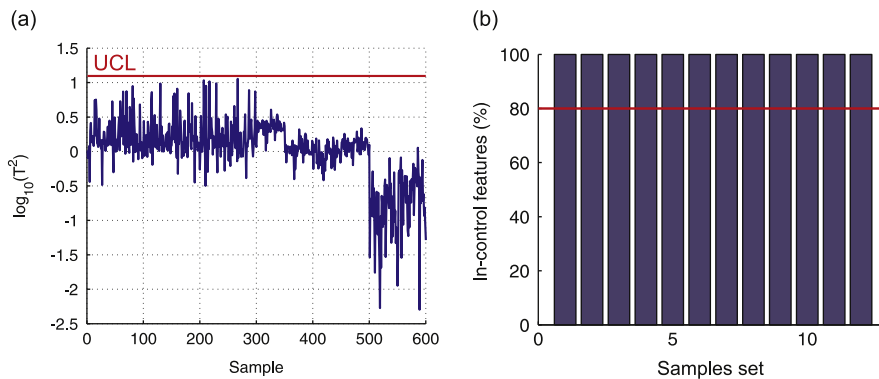

Fig. 27. Automated damage detection in local filter (12:16). (a) Hotelling T^2 control chart, (b) damage alarms.
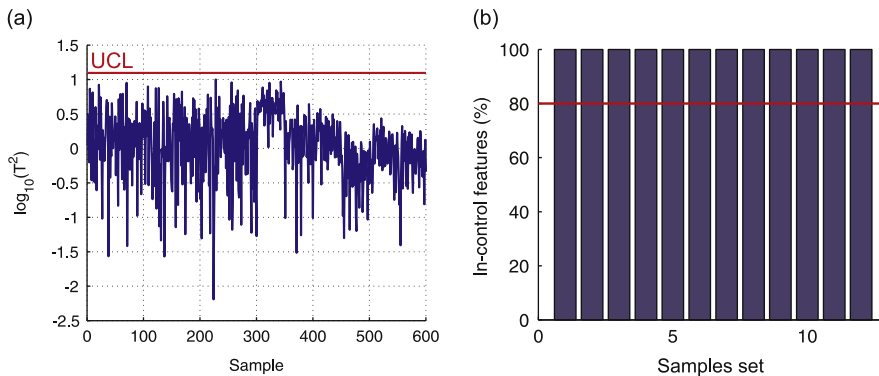

Fig. 28. Automated damage detection in local filter (16:20). (a) Hotelling T^2 control chart, (b) damage alarms.

4. Conclusion

This paper presents two experimental applications of a new technique for unsupervised data-based damage localization using ambient dynamic strain measurements. This output-only method relies on a large network of dynamic strain sensors and a very efficient signal processing technique based on grouping of sensors in several small and independent local filters. In each local filter, the data processing consists of (i) a linear combination of the sensors time histories, (ii) the computation of the power spectral density of the resulting signal, and (iii) the extraction of a damage sensitive feature in given frequency bands. The automation of damage localization is possible by applying univariate or multivariate control charts on the extracted damage sensitive features. In the present work, a novel damage sensitive feature has been proposed, of which the main advantage with respect to the one previously used is that it grows monotonically with the damage.

The performances of the proposed method have been illustrated on a small cantilever plate and a large steel I-beam both equipped with a network of cheap PVDF film sensors. In both cases, the technique has shown excellent performances since all the damage scenarios have been correctly located without false alarms. The results have also highlighted the need for a certain level of overlap between the local filters in order to avoid missing alarms.

The damage introduced in both tests is a "false" damage by fixing a small removable damage device at different positions, and while it has been shown to reproduce accurately a local change of strains in the mode shapes, further tests are needed with a real damage in order to fully validate the technique. Since it is particularly difficult to relate the removable damage device to a specific level of damage, only one prototype of the removable damage device has been tested for each case study, and the increase of the new damage sensitive feature with the level of damage has therefore not yet been illustrated experimentally. Another important issue for the practical implementation is the strain sensing technology which needs to be scaled to bigger structures with a special attention on the high sensitivity required in ambient vibration applications, as well as on the environmental effects. Finally, another perspective of the present work is the experimental validation of the adaptive local filters recently proposed in [51], which consists in updating the configuration of the local filters in order to follow the evolution of damage.

References

[1] N.T. Mascia, A.L. Sartori, Identification and analysis of pathologies in bridges of urban and rural roads, *Revista Ingenierá de Construcción* 26 (2011) 5–24.
[2] C. Hellier, *Handbook of Nondestructive Evaluation*, McGraw-Hill, New York, 2003.
[3] U.S. Department of Transportation, Federal Highway Administration, Reliability of Visual Inspection for Highway Bridges, Vol. 1, Final Report, Report FHWA-RD-01-020, 2010.
[4] D. Pines, E. Aktan, Status of structural health monitoring of long-span bridges in the United States, *Progress in Structural Engineering and Materials* 4 (2002) 372–380.
[5] K. Rofidal, U.S. coast guard responds following the collapse of the I-35W bridge in Minnesota, *USCG Reservist* 54 (2007) 26–29.
[6] B.F. Spencer Jr., T.T. Soong, New applications and development of active, semi-active and hybrid control techniques for seismic and non-seismic vibration in the USA, *Proceedings of International Post-SMiRT Conference Seminar on Seismic Isolation, Passive Energy Dissipation and Active Control of Vibration of Structures*, Cheju, Korea, 1999.
[7] W. Patten, R. Sack, Q. He, Controlled semiactive hydraulic vibration absorber for bridges, *Journal of Structural Engineering* 122 (1996) 187–192.
[8] S.W. Doebling, C.R. Farrar, M.B. Prime, A summary review of vibration-based damage identification methods, *The Shock and Vibration Digest* 30 (1998) 91–105.
[9] J.P. Lynch, K.J. Loh, A summary review of wireless sensors and sensor networks for structural health monitoring, *Shock and Vibration Digest* 38 (2006) 91–128.
[10] SensorsMag, Sensors Magazine, ⟨http://www.sensorsmag.com⟩ (accessed 22 July 2013).
[11] G. J Stein, Some recent developments in acceleration sensors, *Measurement Science Review* 1 (2001) 183–186.
[12] E. Reynders, G.D. Roeck, Reference-based combined deterministic-stochastic subspace identification for experimental and operational modal analysis, *Mechanical Systems and Signal Processing* 22 (2008) 617–737.
[13] E. Reynders, M. Schevenels, G.D. Roeck., MACEC 3.1: A Matlab Toolbox for Experimental and Operational Modal Analysis, Report BWM-2010-05, Department of Civil Engineering, K.U. Leuven, 2010.
[14] A. Rytter, *Vibration Based Inspection of Civil Engineering Structures*, University of Aalborg, 1993.
[15] E. Reynders, G.D. Roeck, Damage identification on the Tilff bridge by vibration monitoring using finite element model updating, *Proceedings of Experimental Vibration Analysis for Civil Engineering Structures*, Bordeaux, France, 2005.
[16] E. Reynders, A. Teughels, G.D. Roeck, Finite element model updating and structural damage identification using OMAX data, *Mechanical Systems and Signal Processing* 24 (2010) 1306–1323.
[17] C.P. Fritzen, D. Jennewein, T. Kiefer, Damage detection based on model updating methods, *Mechanical Systems and Signal Processing* 12 (1998) 163–186.
[18] H. Sohn, C.R. Farrar, F. Hemez, D. Shunk, D. Tinemates, B. Nadler, A Review of Structural Health Monitoring Literature from 1996–2001, Los Alamos National Laboratory Report LA-13976-MS, 2004.
[19] O.D. Salawu, Detection of structural damage through changes in frequency: *a review, Engineering Structures* 19 (1997) 718–723.
[20] H. Sohn, Effect of environmental and operational variability on structural health monitoring, *Philosophical Transactions of the Royal Society, Series A: Mathematical, Physical and Engineering Sciences* 365 (2006) 539–560.
[21] B. Peeters, J. Maeck, G. De Roeck, Vibration-based damage detection in civil engineering: *excitation sources and temperature effects, Smart Materials and Structures* 10 (2001) 518–527.

[22] G. Tondreau, A. Deraemaeker, Local modal filters for automated data-based damage localization using ambient vibrations, *Mechanical Systems and Signal Processing* 39 (2013) 162–180.
[23] S.J. Shelley, J.F. Schultze, R.W. Rost, R.J. Allemang, Active vibration control utilizing a discrete modal filter based control technique, *Proceedings of ISMA1992*, Leuven, Belgium, 1992.
[24] G.L. Slater, S.J. Shelley, Health monitoring of flexible structures using modal filter concepts, *Proceedings of SPIE Smart Structures and Materials*, Albuquerque, New Mexico, USA, 1993.
[25] A. Deraemaeker, A. Preumont, Vibration based damage detection using large array sensors and spatial filters, *Mechanical Systems and Signal Processing* 20 (2006) 1615–1630.
[26] A. Deraemaeker, E. Reynders, G.D. Roeck, J. Kullaa, Vibration-based structural health monitoring using output-only measurements under changing environment, *Mechanical Systems and Signal Processing* 22 (2008) 34–56.
[27] C.R. Farrar, S.W. Doebling, P.J. Cornwell, E.G. Straser, Variability of modal parameters measured on the Alamosa canyon bridge, *Proceedings of IMAC XV*, Orlando, FL, USA, 1997.
[28] G. Tondreau, A. Deraemaeker, E. Papatheou, Experimental damage detection using modal filters on an aircraft wing, *Proceedings of Eurodyn2011*, Leuven, Belgium, 2011.
[29] K. Mendrok, T. Uhl, Experimental verification of the damage localization procedure based on modal filtering, *Structural Health Monitoring* 10 (2) (2011) 157–171.
[30] A.K. Pandey, M. Biswas, M.M. Samman, Damage detection from changes in curvature mode shapes, *Journal of Sound and Vibration* 145 (1991) 321–332.
[31] A. Deraemaeker, On the use of dynamic strains and curvatures for vibration based damage localization, *Proceedings of the Fifth European Workshop on Structural Health Monitoring, Sorrento*, Italy, 2010, pp. 835–840.
[32] Y. Gu, L. Long, P. Tan, Surface strain distribution method for delamination detection using piezoelectric actuators and sensors, *Proceedings of 9th International Conference on Damage Assessment of Structures*, Oxford, UK, 2011.
[33] D.C. Montgomery, *Statistical Quality Control: A Modern Introduction*, John Wiley and Sons, New York, 2009.
[34] T.P. Ryan, *Statistical Methods for Quality Improvement*, John Wiley and Sons, New York, 2000.
[35] Q. Zhang, R.J. Allemang, D.L. Brown, Modal filter: concept and application, *Proceedings of IMAC VIII*, Hyatt, Orlando, FL, USA, 1990.
[36] E. Reynders, R. Pintelon, G.D. Roeck, Uncertainty bounds on modal parameters obtained from stochastic subspace identification, *Mechanical Systems and Signal Processing* 22 (2007) 948–969.
[37] D.J. Ewins, *Modal Testing: Theory and Practice*, Research Studies Press LTD, Letchworth, 1984.
[38] A.V. Oppenheim, R.W. Schafer, *Digital Signal Processing*, Prentice-Hall, New Jersey, 1975.
[39] G. Tondreau, A. Deraemaeker, Vibration based damage localization using multi-scale filters and large strain sensor networks, *Proceedings of the Fifth European Workshop on Structural Health Monitoring*, Sorrento, Italy, 2010.
[40] G. Tondreau, A. Deraemaeker, Damage localization in bridges using multi-scale filters and large strain sensor networks, *Proceedings of ISMA2010*, Leuven, Belgium, 2010.
[41] A. Deraemaeker, K. Worden, *New Trends in Vibration Based Structural Health Monitoring, CISM Courses and Lectures*, Vol. 520, Springer, Wien, New York, 2010.
[42] F. de Lorenzo, M. Calabro, Kurtosis: a statistical approach to identify defect in rolling bearings, *Proceedings of 2nd International Conference on Marine Research and Transportation*, Naples, Italy, 2007.
[43] M. Choi, B. Sweetman, Efficient calculation of statistical moments for structural health monitoring, *Journal of Structural Health Monitoring* 9 (2010) 13–24.
[44] H.R. Martin, F. Honarvar, Application of statistical moments to bearing failure detection, *Applied Acoustics* 44 (1995) 67–77.
[45] G. Tondreau, *Damage Localization in Civil Engineering Structures using Dynamic Strain Measurements*, Université libre de Bruxelles, 2013.
[46] G. Tondreau, A. Deraemaeker, Experimental localization of small damages using modal filters, *Proceedings of IMAC XXXI*, Garden Grove, CA, USA, 2013.
[47] Measurement Specialties, ⟨www.meas-spec.com⟩ (accessed 22 July 2013).
[48] SDTools, Structural Dynamic Toolbox, ⟨http://www.sdtools.com⟩ (accessed 22 July 2013).
[49] B. Peeters, G.D. Roeck, One-year monitoring of the Z24-Bridge: *environmental effects versus damage events, Earthquake Engineering and Structural Dynamics* 30 (2001) 149–171.
[50] H. Sohn, M. Dzwonczyk, E.G. Straser, A.S. Kiremidjian, K.H. Law, T. Meng, An experimental study of temperature effect on modal parameters of Alamosa canyon bridge, *Earthquake Engineering and Structural Dynamics* 28 (1999) 879–897.
[51] G. Tondreau, A. Deraemaeker, Multi-scale modal filters for early damage localization, *Proceedings of ISMA2012*, Leuven, Belgium, 2012.